Materials Today Communications 51 (2026) 114868

Contents lists available at ScienceDirect

Materials Today Communications

journal homepage: www.elsevier.com/locate/mtcomm

Development of Ti–Mo–Cu alloys with enhanced antibacterial activity for biomedical application

Yichun Zhu [a], Qiang Li [a,*], Hu Zhao [a], Xuyan Liu [a], Hao Wang [b], Masaaki Nakai [c], Kenta Yamanaka [d], Mitsuo Niinomi [a,d,e], Ryosuke Ozasa [e], Takayoshi Nakano [e]

[a] School of Mechanical Engineering, University of Shanghai for Science and Technology, Shanghai 200093, PR China
[b] Co-Creation Institute for Advanced Materials, Shimane University, 1060 Nishi-Kawatsu-cho, Matsue, Shimane 690–8504, Japan
[c] Laboratory for Biomaterials and Bioengineering, Institute of Integrated Research, Institute of Science Tokyo, 2–3–10 Kanda-Surugadai, Chiyoda-ku, Tokyo 101–0062, Japan
[d] Institute for Materials Research, Tohoku University, 2–1–1, Katahira, Aoba-ku, Sendai 980–8577, Japan
[e] Division of Materials and Manufacturing Science, Graduate School of Engineering, The University of Osaka, 2–1, Yamadaoka, Suita, Osaka 565–0871, Japan

ARTICLE INFO

Keywords:
Ti–Mo–Cu alloys
Microstructure
Superelasticity
Corrosion resistance
Antibacterial activity

ABSTRACT

To advance the performance of Ti alloys for biomedical applications, Cu—a β-stabilizing element—was incorporated into a Ti–Mo alloy to synergistically achieve desirable mechanical properties and enhanced antibacterial activity. Ti–6Mo–(0, 1, 3, 5, 7)Cu ingots were fabricated via high-vacuum non-consumable arc melting, followed by homogenization treatment and hot rolling into sheets. Specimens for characterization and testing were cut from the sheets and subsequently solution-treated. Phase composition was analyzed using X-ray diffraction, and microstructure was observed by optical microscopy and transmission electron microscopy. Mechanical properties were determined via conventional tensile test, while superelasticity was evaluated through cyclic loading-unloading test. Corrosion resistance was assessed by potentiodynamic polarization measurement, and antibacterial activity was investigated using *E. coli* and *S. aureus* as the test strains, with commercially pure Ti serving as the control group. The results demonstrate that Cu addition enhances β-phase stability, inducing a phase composition shift from α'- and α"-phases to a dominant β-phase. Stress-induced martensitic transformation was observed in the Ti–6Mo–7Cu alloy, which exhibited a superelastic recovery rate of up to 2.4 %. All Ti–Mo–Cu alloys displayed self-passivation behavior, with a passivation current density below 12.00 $\mu A \cdot cm^{-2}$. The released Cu^{2+} concentration was approximately 6.94 $\mu g \cdot L^{-1}$ after 24 h of immersion in PBS, while it reached ~23.44 $\mu g \cdot L^{-1}$ after 168 h of immersion—meeting the biosafety requirements. Antibacterial efficiency was greatly improved with increasing Cu content. Specifically, the Ti–6Mo–7Cu alloy achieved antibacterial rates of 90.6 % and 79.8 % against *E. coli* and *S. aureus*, respectively, making it a promising candidate for biomedical applications.

1. Introduction

Ti and its alloys possess a low Young's modulus, high corrosion resistance, and excellent biocompatibility, rendering them ideal biomedical implant materials for clinical applications. In the late 1970s, the Ti–6Al–4V alloy—initially developed for aerospace applications—was widely adopted in joint repair. Its mechanical strength and corrosion resistance surpass those of commercially pure titanium (CP Ti), making it a superior alternative at the time. However, long-term implantation of Ti–6Al–4V in living organisms can result in the release of vanadium ions. Given that vanadium is potentially cytotoxic, prolonged accumulation of these ions in the human body may give rise to various adverse health effects [1].

To address advanced biomedical requirements, β-type Ti alloys that are free of toxic elements and possess lower Young's moduli have emerged as the current research focus. The mainstream β-type Ti alloy systems primarily include Ti–Mo-based and Ti–Nb-based alloys. By optimizing the contents of alloying elements, researchers can regulate the phase composition to achieve diverse combinations of mechanical properties—such as high strength, low Young's modulus, superelasticity, and shape memory effect. The widely utilized binary Ti–15Mo alloy, first developed by Britain's IMI in 1958 and standardized under ASTM

* Corresponding author.
E-mail addresses: liqiang@usst.edu.cn, jxli@tju.edu.cn (Q. Li).

https://doi.org/10.1016/j.mtcomm.2026.114868
Received 7 December 2025; Received in revised form 21 January 2026; Accepted 13 February 2026
Available online 14 February 2026

F2066, retains fine β grains following solution treatment at 800°C. This alloy exhibits a low Young's modulus, high ductility, and excellent corrosion resistance, thereby rendering it well-suited for orthopedic implant applications [2]. Takemoto et al. reported that the solution-treated Ti–6Mo alloy exhibits a relatively low Young's modulus among binary Ti–Mo alloys [3]. A series of Ti–6Mo-based alloys have been developed, including Ti–6Mo–4Cr [4], Ti–6Mo–4Sn [5], Ti–6Mo–3Fe–5Ta [6], and Ti–6Mo–6Nb–12Sn [7].

Unfortunately, widely used Ti-based implants (e.g., CP Ti and Ti–6Al–4V) lack inherent antibacterial properties, while Ti–Mo alloys only demonstrate moderate antibacterial activity. Both of these shortcomings increase the risk of post-surgical bacterial infections in patients [8]. Bacterial colonization on implant surfaces proceeds through four sequential stages: initial adhesion and proliferation, biofilm formation, maturation, and dispersion [9]. Biofilms shield encapsulates bacteria from antibiotics and the host's immune system, thereby enhancing bacterial survival and persistence [10]. Owing to such biofilm-mediated protection and the rising prevalence of bacterial antibiotic resistance, strategies relying solely on antibiotics for infection prevention are suboptimal and frequently ineffective [11]. Thus, the development of implants with intrinsic antibacterial properties—designed to inhibit bacterial adhesion, proliferation, and biofilm formation on their surfaces—is of paramount importance [9].

Two primary strategies have been established to enhance the antibacterial performance of Ti implants: surface modification and the incorporation of antibacterial alloying elements [12]. The preparation of coatings loaded with antibacterial agents—based on currently used Ti implants—has been extensively explored [13]; however, several challenges remain, including achieving coatings with excellent mechanical properties, strong adhesion between the coating and substrate, and desirable antibacterial durability [9]. Ag and Cu are two well-recognized feasible alloying elements that can be incorporated into Ti alloys to improve their antibacterial activity [14]. Although Ag-added Ti alloys have been proved to exhibit strong and stable antibacterial activity, concerns persist regarding their potential in vivo toxicity, as reported in existing studies [15]. Fortunately, copper (Cu) is an essential trace metal for human physiological functions and metabolic processes. Numerous studies have demonstrated that Cu ions possess broad-spectrum antibacterial properties; incorporating Cu as an alloying element into Ti alloys can simultaneously enhance antibacterial performance and corrosion resistance [16,17]. Animal experiments have further confirmed that Ti–Cu alloys exhibit superior osseointegration and lower bone resorption rates compared to CP Ti [18]. Additionally, Cu acts as a β-phase stabilizing element in Ti alloys, expanding the β-phase region and optimizing mechanical properties. However, excessive Cu addition greatly impairs ductility and may induce cytotoxicity [17].

Since conventional Ti–Mo alloys exhibit limited antibacterial activity, Cu addition is a feasible strategy to enhance their antibacterial performance. Although numerous studies have been conducted on Cu-containing antibacterial Ti alloys, the effects of Cu on the mechanical properties, corrosion resistance, and antibacterial activity of Ti–Mo-based alloys remain insufficiently investigated. Considering the efficacy of Cu in regulating β-phase stability, the Mo content was fixed at 6 % (mass%; hereafter referred to as mass% unless otherwise specified) to retain the feasibility of tailoring β-phase stability via Cu addition. A series of Ti–6Mo–xCu (x = 0, 1, 3, 5, 7) ternary alloys were fabricated and systematically characterized to investigate the effects of Cu content on their microstructure, deformation behavior, mechanical properties, corrosion resistance, and antibacterial properties. By tailoring the Cu content in a controlled manner, this study realizes the regulation of phase composition and the integration of multiple functionalities. In doing so, it addresses the existing research gap in the synergistic optimization of multi-performance metrics for Ti–Mo-based alloys, while providing novel insights and practical strategies for the development of advanced biomedical implant materials.

2. Methods

2.1. Preparations

Ti–6Mo–(0, 1, 3, 5, 7)Cu alloy ingots (approximately 50 g) were fabricated using a high-vacuum non-consumable electric arc-melting furnace under an Ar protective atmosphere. To ensure compositional homogeneity, each ingot was subjected to 5 melting cycles, with each cycle consisting of ~300 s of melting, 600 s of cooling, and subsequent flipping. The as-cast ingots were homogenized at 1000 °C for 4 h, followed by hot rolling at 1000 °C to obtain sheets with a final thickness of ~1.8 mm. A wire electrical discharge machine was used to cut the sheets into specimens for various tests. For tensile test, the specimens were dog-bone-shaped sheets with a gauge section of 12 mm × 4 mm, and for other tests, the specimens were square sheets with dimensions of 10 mm × 10 mm. All specimens were then solution-treated at 850 °C for 1 h, followed by water quenching. The surface oxide layers formed after homogenization, hot rolling, cutting, and solution treatment were sequentially removed by grinding with sandpapers.

2.2. Phase and microstructure characterizations

Phase compositions were analyzed using a Bruker D8 Advance X-ray diffractometer (XRD) with Cu Kα radiation under a voltage of 40 kV, a current of 40 mA, a scanning speed of 0.1°/s, and a step of 0.02°. Microstructural observations were conducted using a GX-4XC optical microscope (OM). Prior to observation, the specimens were embedded in epoxy resin, ground with 80–2000# sandpapers, polished to a mirror using a SiO_2 suspension, and finally etched in a mixed acid solution with a volume ratio of $HF:HNO_3:H_2O = 3:15:82$ for 15–30 s. Additionally, the specimens were mechanically polished to a thickness of ~50 μm, dimpled with a phosphor bronze ring to ~15 μm, and ion-milled to obtain electron-transparent thin foils. They were subsequently characterized using a JEOL JEM-2000EX transmission electron microscope (TEM) operating at an accelerating voltage of 200 kV.

2.3. Tensile tests

Two types of tensile tests were performed using a universal testing machine equipped with a fixed strain gauge at room temperature (~25 °C), under a crosshead speed of 8.33×10^{-3} mm·s^{-1}. To determine the basic mechanical properties, a monotonic load was applied until specimen fracture. To evaluate the superelasticity, cyclic loading-unloading tests were conducted, where the applied strain was incrementally increased from 1.0 % to the fracture strain in 1.0 % steps per cycle.

2.4. Electrochemical corrosion tests

Corrosion resistance was evaluated using a Gamry Interface 1000 electrochemical workstation in a 0.9 % NaCl solution. A three-electrode system was employed, comprising the alloy specimen as the working electrode, a Pt sheet as the counter electrode, and a saturated calomel electrode (SCE) as the reference electrode. Prior to electrochemical measurements, the open-circuit potential (E_{ocp}) was monitored for 1 h by immersing the specimen in the electrolyte without applying an external potential. Subsequently, potentiodynamic polarization tests were performed over a potential range of –0.5 to 3 V (vs. E_{ocp}) at a scan rate of 1 mV·s^{-1}.

2.5. Ion release test

Square alloy specimens were immersed in 15 mL of phosphate-buffered saline (PBS) and statically incubated in a constant-temperature chamber at 37 °C for 24 h. Separately, the Ti–6Mo–7Cu alloy was subjected to the identical immersion procedure for extended durations of 72, 120, and 168 h, respectively. After incubation, the

concentration of Cu^{2+} ions released into the PBS solution was quantified using a Thermo Fisher iCAP 7400 inductively coupled plasma mass spectrometer (ICP-MS).

2.6. Antibacterial properties

Gram-negative *E. coli* (ATCC 25922) and Gram-positive *S. aureus* (ATCC 6538) were selected as the test strains to evaluate the antibacterial performance of Ti–6Mo–(0, 1, 3, 5, 7)Cu alloys, with serving CP Ti as the control group. The antibacterial tests were conducted following the broth dilution-agar plate counting method. The alloy specimens were individually placed into sterile 15-mL centrifuge tubes, and then 10 mL of Mueller-Hinton liquid medium and 100 μL of bacterial suspension were added to each tube. The tubes were transferred to a 37 °C constant-temperature shaker and incubated for 24 h. After incubation, the bacterial suspensions were serially diluted 10^7 times. A 100 μL aliquot of the diluted bacterial suspension from each tube was pipetted onto the center of a solid nutrient broth agar plate in a 100-mm diameter Petri dish. The bacterial suspension was then uniformly spread across the agar surface using a sterile spreader, followed by incubation at 37 °C for 24 h. The antibacterial rate of the alloy was calculated by the following formula:

$$X = \left(1 - \frac{N_E}{N_C}\right) \times 100\% \quad (1)$$

where, X denotes the antibacterial rate, N_E is the colony number of the tested alloy group, and N_C is the colony number of the control group.

3. Results

3.1. Phases compositions and microstructures

The XRD patterns of solution-treated Ti–6Mo–(0, 1, 3, 5, 7)Cu alloys are presented in Fig. 1, and their corresponding OM images are shown in Fig. 2. For Ti–6Mo, XRD analysis revealed diffraction peaks corresponding to α'-martensite and α"-orthorhombic phases, while OM observations showed a uniform acicular microstructure across the entire specimen (Fig. 2a). These results are consistent with the findings reported by Ho et al. [19], confirming that Ti–6Mo primarily consists of α'- and α"-phases.

With the addition of 1 % Cu, the relative diffraction intensity of the α'-phase decreased. When the Cu content was increased to 3 %, the diffraction peak around 38.62° broadened. Since the $(110)_\beta$ diffraction peak is located at 39.48°, this broadening was attributed to the retention of β-phase during water quenching. However, minimal microstructural differences were observed among the Ti–6Mo–(0, 1, 3)Cu alloys (Fig. 2a–c), all of which exhibited a nearly full acicular structure. These observations indicate that the β-phase stability of these three alloys is limited, allowing the martensitic transformation to proceed completely during quenching [20].

As the Cu content further increased to 5 %, the β-phase diffraction peaks intensified. OM image showed that acicular structures randomly distributed within β grains (Fig. 2d), which is a typical α" + β dual-phase microstructure for solution-treated metastable β-type Ti alloys.

For Ti–6Mo–7Cu, prominent β-phase diffraction peaks were observed, accompanied by a weak ω-phase peak around 79.40°. Neither α' nor α" phases were observed in the XRD pattern or OM images, indicating that the martensitic transformation start temperature (M_s) of this alloy is below room temperature [2]. Since ω-phases exist as nanosized particles, they are not resolvable via OM [6]. Only equiaxed β grains were observed in the OM image of Ti–6Mo–7Cu (Fig. 2e).

Additionally, Ti–6Mo–7Cu was subjected to TEM characterization to directly verify the existence and nanoscale morphology of the constituent phases, as presented in Fig. 3. Second-phase particles were barely detected in the bright-field image (Fig. 3a). Diffraction spots corresponding to the ω-phase were identified in the selected area electron diffraction (SAED) patterns. Furthermore, nano-sized ω-phase domains were observed in the dark-field image (Fig. 3b), confirming the existence of ω-phase in the alloy.

Fig. 4 presents the XRD patterns of Ti–6Mo–(0, 1, 3, 5, 7)Cu alloys subsequent to monotonic tensile tests. For the Ti–6Mo–(0, 1, 3)Cu alloys, minimal changes were observed in their XRD patterns after deformation. In contrast, for the Ti–6Mo–5Cu and Ti–6Mo–7Cu alloys, the relative intensity of the α"-phase diffraction peak increased noticeably. Especially, for Ti–6Mo–7Cu, the diffraction intensity of the α"-phase exceeded that of the β-phase, indicating that the α"-phase became the dominant phase following tensile deformation.

The microstructural changes observed after the monotonic tensile

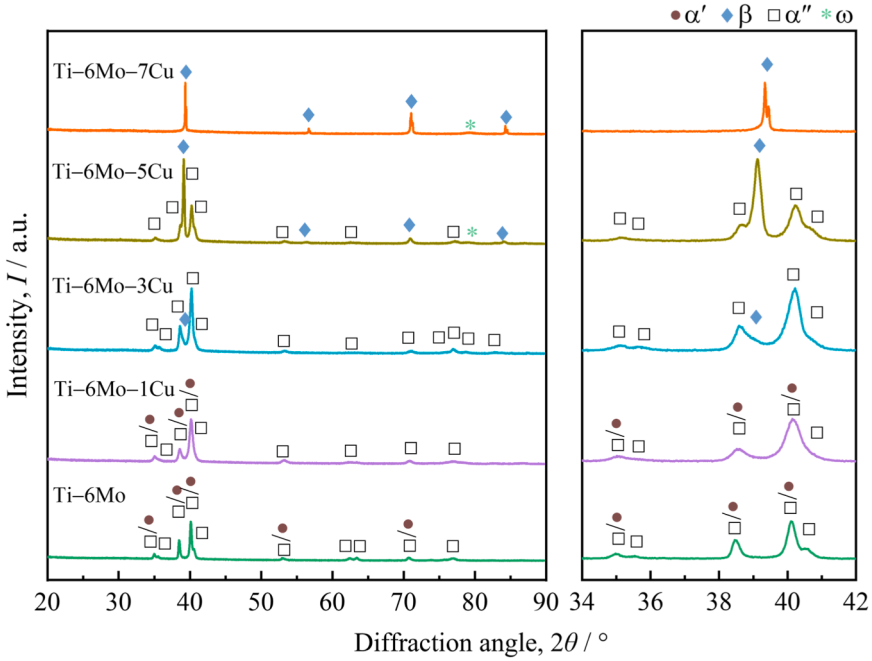

Fig. 1. XRD patterns of the solution-treated Ti–6Mo–(0, 1, 3, 5, 7)Cu alloys.

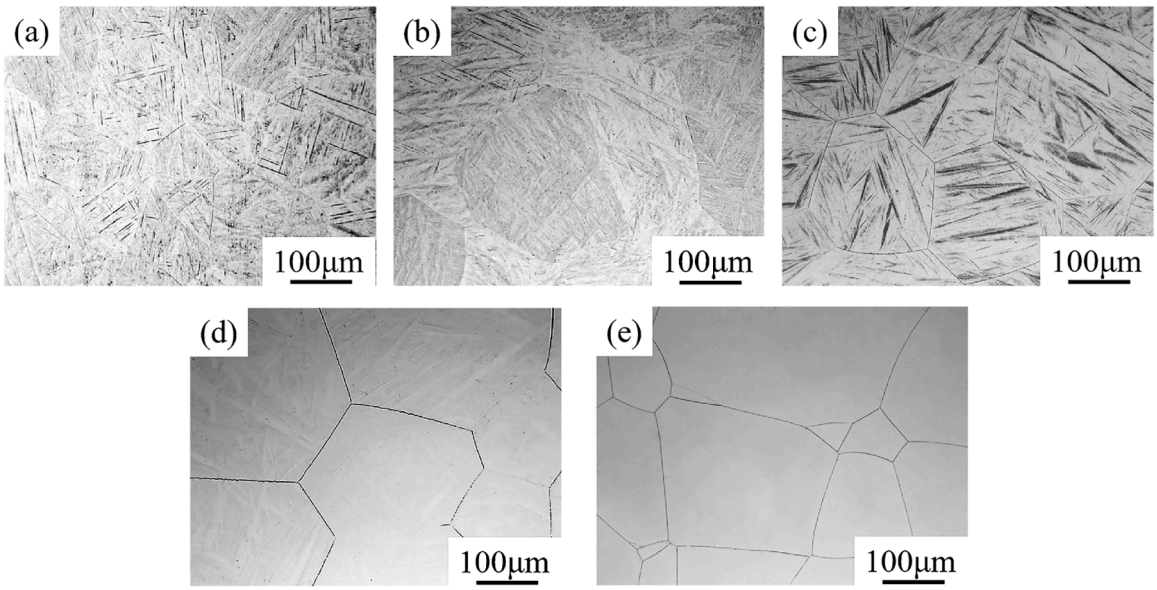

Fig. 2. OM images of the solution-treated Ti–6Mo–(0, 1, 3, 5, 7)Cu alloys: (a) Ti–6Mo; (b) Ti–6Mo–1Cu; (c) Ti–6Mo–3Cu; (d) Ti–6Mo–5Cu; (e) Ti–6Mo–7Cu.

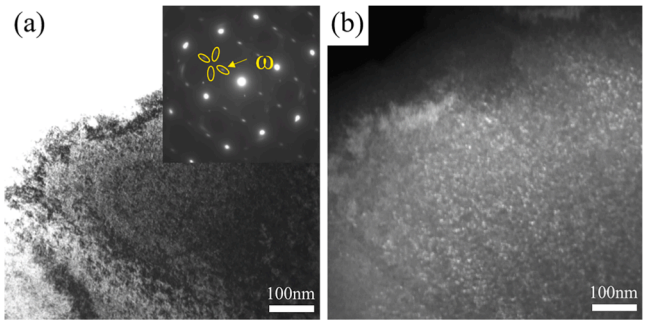

Fig. 3. TEM results of the Ti–6Mo–7Cu alloy: (a) bright-field image with SEAD pattern; (b) bright-field image. Beam direction is parallel to $[110]_{\beta}$ and $[1120]_{\omega}$.

tests were consistent with the XRD results, as illustrated in Fig. 5. The microstructures of the deformed Ti–6Mo–(0, 1, 3)Cu alloys remained nearly identical to those of the solution-treated ones. For Ti–6Mo–5Cu, both the solution-treated and deformed states consisted of an α" + β dual-phase structure with the β-phase as the matrix; thus, noticeable microstructural changes were hardly observed after tension. In the case of Ti–6Mo–7Cu after tensile deformation, the β grains were characterized by numerous lamellar structures. These lamellae varied in thickness across different grains but maintained uniform dimensions and parallel orientations within individual grains. Originating at grain boundaries, the lamellae extended through the entire β grain and terminated at the opposing boundaries. Additionally, fine V-shaped needle-like structures occasionally appeared among the parallel lamellae, confirming that stress-induced martensitic transformation (SIMT) from β to α" occurred during tensile deformation [21].

3.2. Mechanical properties

The tensile engineering stress-strain curves of the solution-treated Ti–Mo–Cu alloys are presented in Fig. 6a, while the mechanical properties derived from tensile tests are summarized in Fig. 6b. Since a distinct yield plateau was barely observable in these alloys, the 0.2 % proof stress ($\sigma_{0.2}$) was determined alongside the ultimate tensile strength (σ_b), Young's modulus (E), and percentage elongation after fracture (ε_l) from the stress-strain curves. Ti–6Mo and Ti–6Mo–1Cu exhibited analogous tensile behaviors, encompassing elastic deformation, yielding, uniform plastic deformation, necking, and fracture. Following yielding, the stress increased moderately before declining upon the onset of necking. In contrast, Ti–6Mo–3Cu displayed a notable stress increment post-yielding, indicative of enhanced work hardening capacity; similarly, the stress gradually decreased after reaching the maximum value, confirming the occurrence of necking. Although Ti–6Mo–5Cu demonstrated further improved work hardening ability, it fractured directly during the work hardening stage, suggesting compromised plastic deformation capacity. Ti–6Mo–7Cu exhibited a typical double-yielding behavior: the first yield is generally attributed to the occurrence of SIMT during tension, while the second yield corresponds to the yielding of the β-phase [22]. Furthermore, Ti–6Mo–7Cu underwent substantial plastic deformation prior to fracture.

The mechanical properties of the alloys were strongly influenced by their phase compositions. The α'-phase is typically brittle, whereas the α"-phase is a ductile phase [3,4]. The mixture of α'- and α"-phases endowed Ti–6Mo with a $\sigma_{0.2}$ of ~543.7 MPa, an σ_b of ~739.2 MPa, and an ε_l of ~21.1 %, which is consistent with the results reported by Cardoso et al. [23]. As noted earlier, Ti–6Mo–1Cu exhibited a phase composition and microstructure analogous to Ti–6Mo, leading to nearly identical mechanical properties. When 3 % Cu was added, the volume fraction of the α'-phase decreased, and the β-phase emerged. Compared to the α'-phase, the β-phase is softer and more ductile; consequently, Ti–6Mo–3Cu was more susceptible to yielding, resulting in a reduced $\sigma_{0.2}$. The three-phase (α', α", and β) structure of Ti–6Mo–3Cu increased the density of phase boundaries, which hindered dislocation slip and thereby enhanced work hardening capacity. Since both the α"-phase and β-phase are ductile, the plasticity of the alloy remained largely uncompromised. When the Cu content was increased to 5 %, the brittle ω-phase formed, leading to increased $\sigma_{0.2}$ and σ_b accompanied by a decrease in ε_l. For Ti–6Mo–7Cu, the first yielding occurred at a low stress level due to SIMT [22], resulting in a $\sigma_{0.2}$ as low as ~262.9 MPa. With further strain accumulation, elastic deformation of both the α"- and β-phases took place, causing a subsequent rise in stress [24]. The second yielding, corresponding to the yielding of the β-phase [25], was approximately 773.5 MPa, and the σ_b reached ~835.9 MPa, indicating superior strength. As Ti–6Mo–7Cu was predominantly composed of the ductile β-phase, its ε_l increased to ~25.1 %.

The E of the alloys is mainly dependent on the constituent phases and their volume fractions. In Ti alloys, the ω-phase typically exhibits the highest modulus among all phases; the α'-phase has a moderate

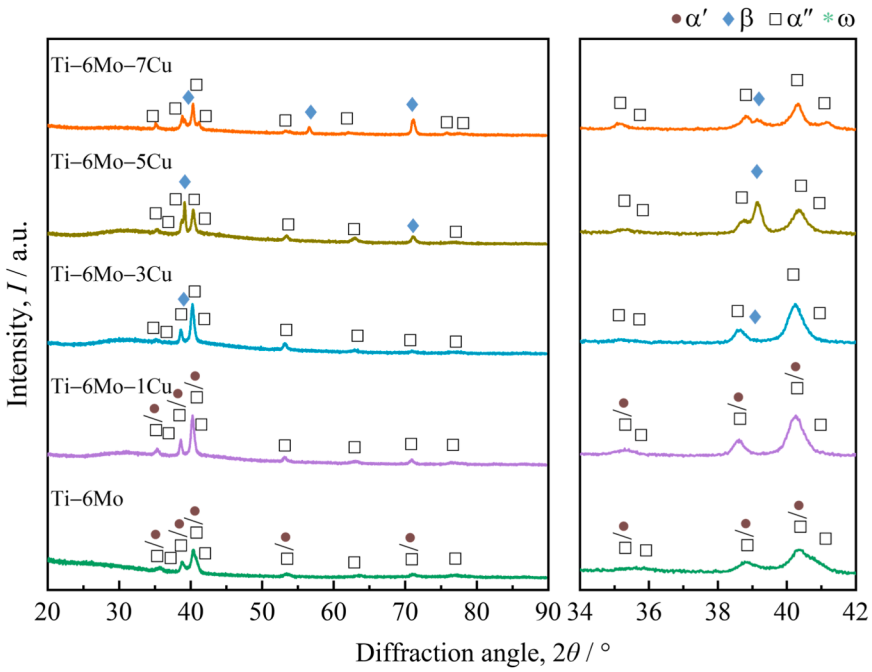

Fig. 4. XRD patterns of the Ti–6Mo–(0, 1, 3, 5, 7)Cu alloys after monotonic tensile deformation.

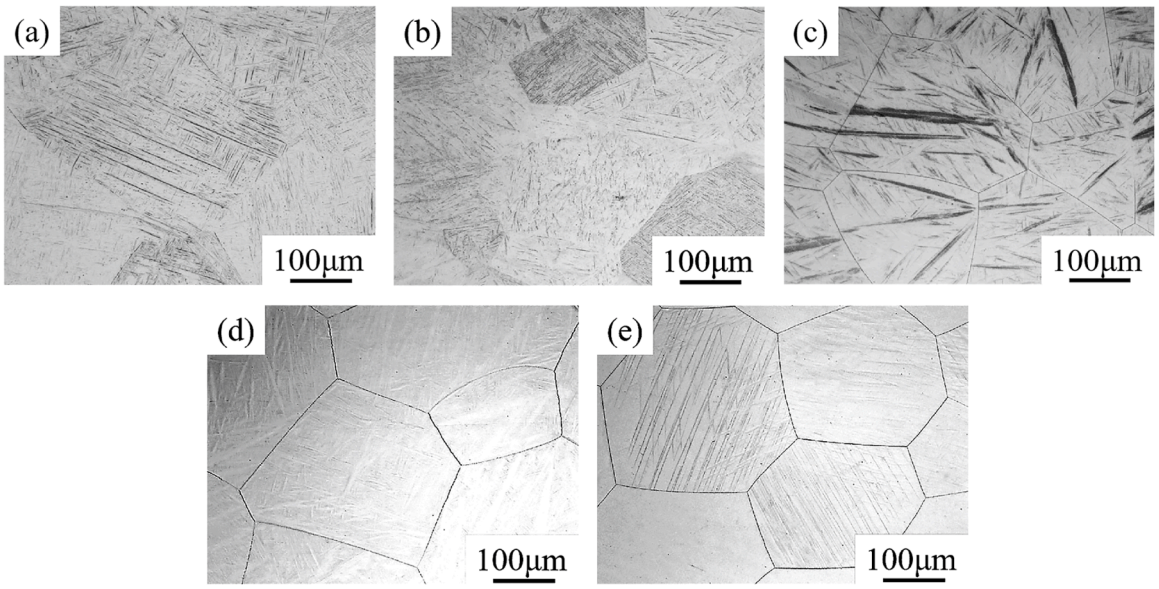

Fig. 5. OM images of the Ti–6Mo–(0, 1, 3, 5, 7)Cu alloys after monotonic tensile deformation: (a) Ti–6Mo; (b) Ti–6Mo–1Cu; (c) Ti–6Mo–3Cu; (d) Ti–6Mo–5Cu; (e) Ti–6Mo–7Cu.

modulus, close to that of the α-phase; the α"-phase shows a slightly lower modulus; and the metastable β-phase generally displays the lowest modulus [3]. In the present study, the variation of *E* followed this general trend. Ti–6Mo, composed of α'+ α"-phases, exhibited an *E* of ~75.3 GPa. As the volume fraction of the α'-phase decreased in Ti–6Mo–1Cu, its *E* slightly declined. With a further increase in Cu content, the volume fractions of both α'- and α"-phases decreased, and the ω-phase precipitated. For Ti–6Mo–5Cu, *E* increased noticeably, attributed to the increased volume fraction of the ω-phase. Since the β-phase became the dominant phase in Ti–6Mo–7Cu, *E* slightly decreased.

3.3. *Superelasticity*

The cyclic loading-unloading curves of the solution-treated Ti–6Mo–(0, 1, 3, 5, 7)Cu alloys are presented in Fig. 7a–e, while the recovery strains as a function of applied strain are summarized in Fig. 7f. The number of cycles to failure depended on the ε_l of the alloys, which is a direct reflection of their deformation capacity. For Ti–6Mo, the recovery strain initially increased with increasing applied strain, reaching a maximum of ~1.3 % at an applied strain of 14.0 %. Beyond this point, the recovery strain decreased with further increases in applied strain. Ti–6Mo–1Cu exhibited a maximum recovery strain of ~1.9 % at an applied strain of 17.0 %, whereas Ti–6Mo–3Cu achieved a peak recovery strain of ~2.0 % at applied strains of 15.0 % and 16.0 %. A similar

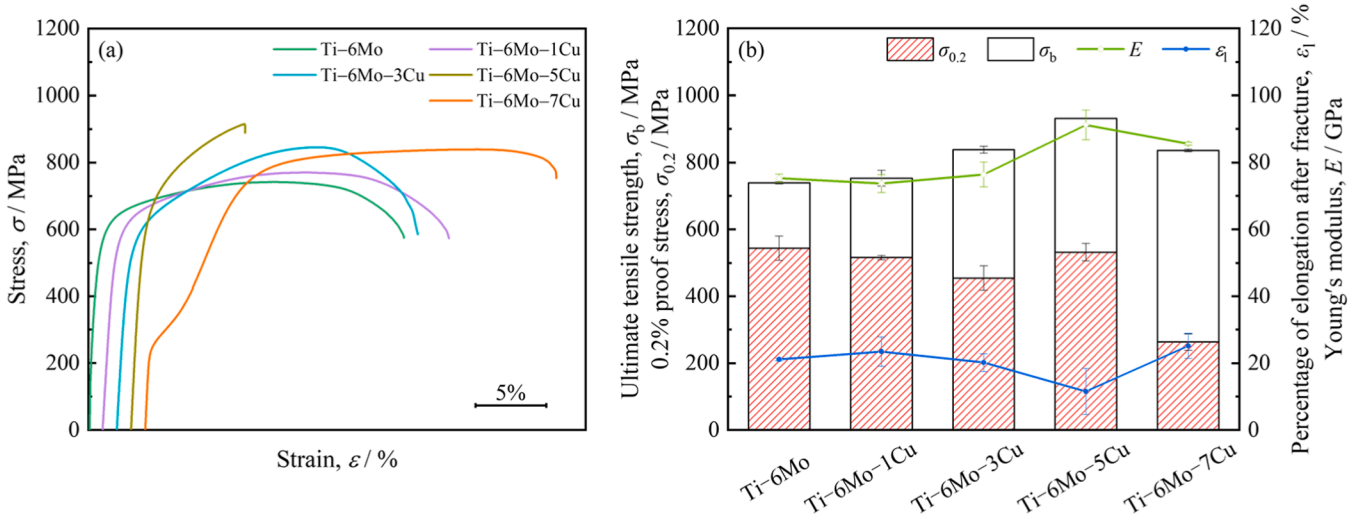

Fig. 6. Tensile engineering stress-strain curves (a) and mechanical properties (b) of the solution-treated Ti–6Mo–(0, 1, 3, 5, 7)Cu alloys.

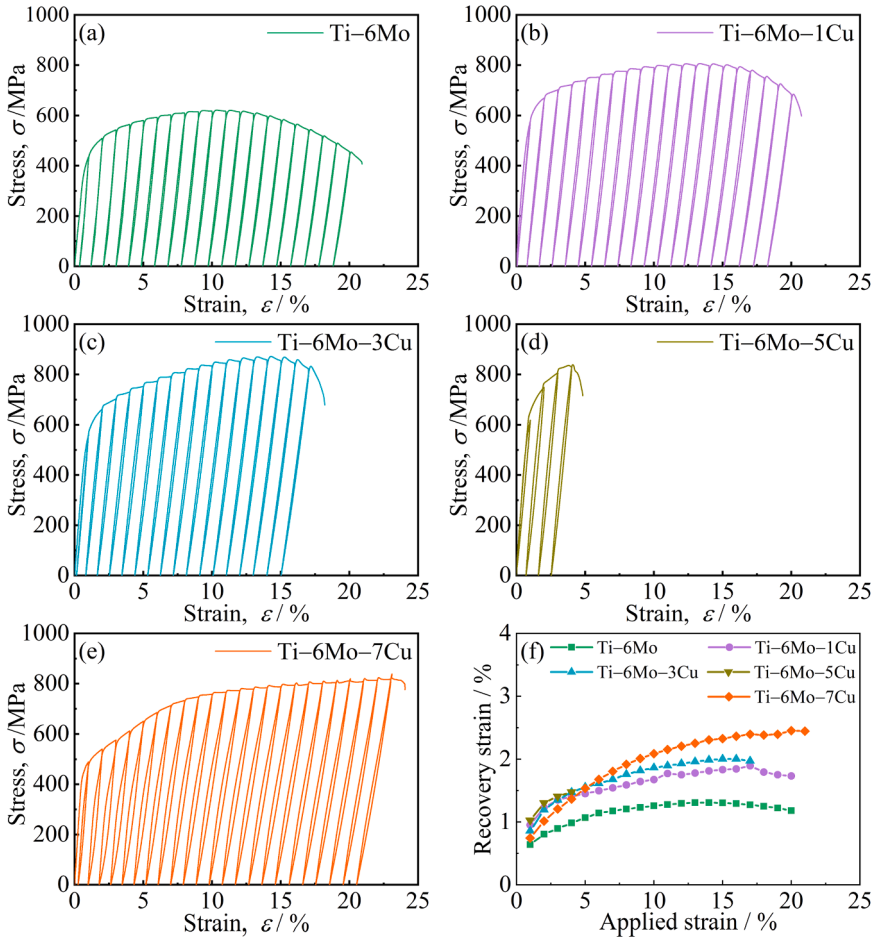

Fig. 7. Cyclic loading-unloading curves of Ti–Mo–Cu alloys: (a) Ti–6Mo; (b) Ti–6Mo–1Cu; (c) Ti–6Mo–3Cu; (d) Ti–6Mo–5Cu; (e) Ti–6Mo–7Cu; (f) recovery strain of the alloys in each cycle.

decreasing trend in recovery strain was observed for both Ti–6Mo–1Cu and Ti–6Mo–3Cu after attaining their respective maximum values. Notably, necking occurred precisely at the applied strain corresponding to the maximum recovery strain. Following necking, localized deformation emerged, accompanied by a reduction in deformation resistance; the accumulation of localized deformation consequently led to a decrease in the recoverable strain of the samples.

Due to its direct fracture during the work hardening stage, Ti–6Mo–5Cu failed after the fifth loading cycle, which corresponded to a maximum recovery strain of ~1.5 %. Ti–6Mo–7Cu exhibited an ε_l of up to ~25.1 %, enabling it to withstand more than 20 cyclic loading-unloading cycles. Furthermore, its recovery strain increased

progressively with the gradual application of strain, reaching a maximum of 2.4 % during the final cycle. This behavior is attributed to the fact that necking in Ti–6Mo–7Cu only occurred at the maximum applied strain.

3.4. Corrosion behaviors

The Ti–6Mo–(0, 1, 3, 5, 7)Cu alloys exhibited analogous potentiodynamic polarization curves, as illustrated in Fig. 8, indicating similar electrochemical behaviors among the series. For Ti–6Mo, when the applied potential exceeded its self-corrosion potential (E_{corr}, approximately –0.43 V vs. SCE; hereafter, all potentials refer to SCE unless otherwise specified), the current density increased gradually until the applied potential reached –0.10 V. Subsequently, the current density stabilized at approximately 7.64 μA·cm^{-2}, signifying the alloy transited into the passivation stage. At this stage, a stable passive film formed on the alloy surface, which is responsible for the material's corrosion resistance [26]. Similar passivation behavior was observed for the Ti–6Mo–(1, 3, 5, 7)Cu alloys when the applied potential exceeded ~0.20 V. Since all alloys exhibited passivation during anodic polarization, the E_{corr} and passivation current density (i_{pp}) were selected as the key parameters to evaluate corrosion resistance, as summarized in Table 1. The addition of Cu induced a positive shift in E_{corr}, indicating a reduced corrosion tendency. With increasing Cu content up to 5 %, the i_{pp} increased to approximately 11.98 μA·cm^{-2}. Notably, the i_{pp} of Ti–6Mo–7Cu decreased and was slightly lower than that of Ti–6Mo.

When the applied potential was further increased, pitting corrosion occurred in all alloys, with noticeable differences in current density observed among them. For Ti–6Mo, the current density began to increase when the applied potential reached approximately 1.50 V. Notably, it subsequently decreased and finally stabilized once the applied potential was raised to ~1.70 V, indicating that the sample entered the secondary passivation stage. The passive films of the Ti–6Mo–(1, 3)Cu alloys became unstable at approximately 1.35 V, with secondary passivation initiating at around 1.81 V. For the Ti–6Mo–(0, 1, 3)Cu alloys, the current densities during secondary passivation were higher than those during initial passivation, suggesting that the stability of the newly formed passive film was inferior to that of the primary passive film [27]. The Ti–6Mo–(5, 7)Cu alloys exhibited a pitting potential of ~1.44 V. At an applied potential of ~1.82 V, the current density of Ti–6Mo–5Cu reached approximately 95.92 μA·cm^{-2}; although it decreased slightly thereafter, a continuous increase was observed with further elevation of the applied potential. In contrast, Ti–6Mo–7Cu showed a stable current density of approximately 11.04 μA·cm^{-2} at ~1.63 V, which also increased continuously as the applied potential exceeded ~2.04 V. These phenomena indicate that stable secondary passivation is difficult to achieve in these two alloys.

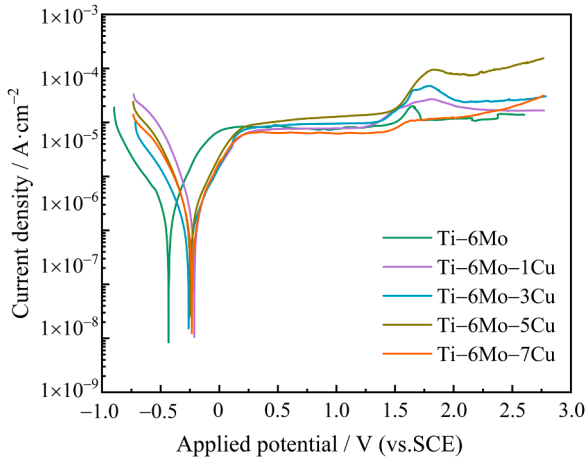

Fig. 8. Potentiodynamic polarization curves of the Ti–6Mo–(0, 1, 3, 5, 7) Cu alloys.

Table 1
Electrochemical parameters of the Ti–6Mo–(0, 1, 3, 5, 7)Cu alloys derived from potentiodynamic polarization curves.

Samples	E_{corr} (V, vs. SCE)	i_{pp} (μA·cm^{-2})
Ti–6Mo	–0.43	7.64
Ti–6Mo–1Cu	–0.22	7.81
Ti–6Mo–3Cu	–0.26	9.67
Ti–6Mo–5Cu	–0.25	11.98
Ti–6Mo–7Cu	–0.23	6.19

3.5. Cu^{2+} release behaviors

After immersion in PBS for 24 h, Cu^{2+} ions were released from the alloy substrates into the solution. As illustrated in Fig. 9a, the Cu^{2+} concentration in the solution exhibited a nearly linear increase with increasing Cu content in the alloys. Additionally, for Ti–6Mo–7Cu, the Cu^{2+} concentration was approximately 6.94 μg·L^{-1} after 24 h of immersion, which is much lower than that (~23 μg·L^{-1}) detected in the Ti–35Nb–4Cu alloy [28]. Meanwhile, the results of extended immersion test on Ti–6Mo–7Cu indicated a time-dependent increase in Cu^{2+} concentration (Fig. 9b), with Cu^{2+} reaching 23.44 μg·L^{-1} after 168 h of immersion. Notably, this value falls within the biosafety range, since a Cu^{2+} concentration below 9 × 10^{3} μg·L^{-1} has been established as safe [29].

3.6. Antibacterial properties

The morphologies of *E. coli* and *S. aureus* colonies corresponding to CP Ti and Ti–6Mo–(0, 1, 3, 5, 7)Cu alloys are presented in Fig. 10 and Fig. 11, respectively. The antibacterial rates of the Ti–Mo–Cu alloys against the two bacterial strains are plotted in Fig. 12. The white spots on the agar plates represent bacterial colonies. For CP Ti, a dense distribution of colonies was observed for both *E. coli* and *S. aureus*, indicating its poor antibacterial activity [16]. A slight reduction in colony density was noted for Ti–6Mo. In contrast, noticeable reductions in bacterial colony counts of both *E. coli* and *S. aureus* were observed in Ti–6Mo–1Cu, demonstrating that Cu addition effectively inhibited the bacterial growth, thereby enhancing antibacterial performance. The antibacterial rates against *E. coli* and *S. aureus* were 60.9 % and 41.3 %, respectively. With increasing Cu content, the colony count gradually decreased, indicating a positive correlation between the antibacterial rate and Cu content. Ti–6Mo–7Cu displayed the highest antibacterial rate of 90.6 % and 79.8 % against *E. coli* and *S. aureus*, respectively, which is comparable to that of other Cu-containing Ti alloys (e.g., Ti–3Cu and Ti–4Cu alloys subjected to solution treatment at 900 °C for 3 h followed by aging treatment at 400 °C for 12 h) [30].

4. Discussion

In Ti alloys, different β-stabilizing elements exhibit varying capacities to stabilize the β-phase. To quantify the contribution of each element to β-phase stabilization, the molybdenum equivalent ($[Mo]_{eq}$) has been proposed and can be calculated using the following formula [31]:

$$[Mo]_{eq} = 1.0Mo + 0.67V + 0.44W + 0.28Nb + 2.9Fe + 1.6Cr + 0.77Cu + 1.11Ni + 1.43Co + 1.54Mn–1.0Al \quad (2)$$

Here, Mo serves as the reference element, with other elements normalized to equivalent Mo values. The coefficient assigned to each element reflects its relative β-stabilizing potency. Despite its long-standing use, this formula remains applicable to the present study.

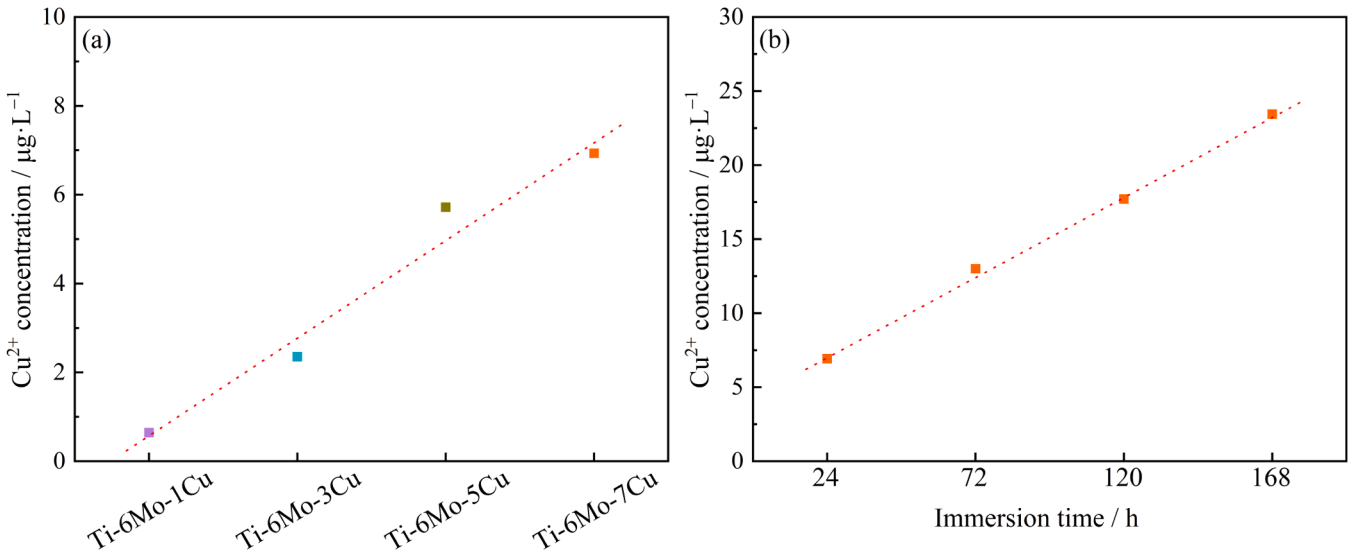

Fig. 9. Cu^{2+} concentrations in PBS for the Ti–Mo–Cu alloys: (a) effect of Cu content on release levels after 24 h of immersion; (b) time-dependent release behavior of Ti–6Mo–7Cu alloy over 168 h.

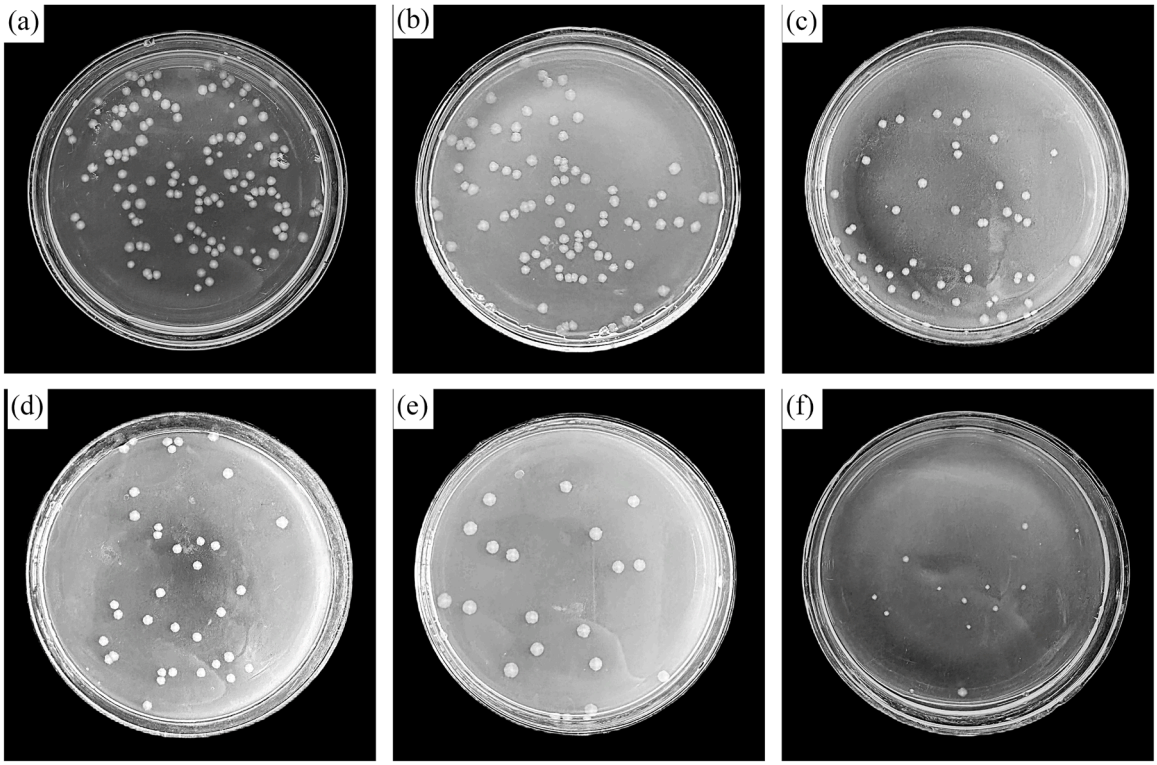

Fig. 10. Morphologies of *E. coli* corresponding to: (a) CP Ti; (b) Ti–6Mo; (c) Ti–6Mo–1Cu; (d) Ti–6Mo–3Cu; (e) Ti–6Mo–5Cu; (f) Ti–6Mo–7Cu.

The $[Mo]_{eq}$ of Ti–6Mo–7Cu is calculated to be 11.39, which is comparable to that of other metastable β-type Ti alloys, such as Ti–12Mo–5Zr, Ti–15Mo–5Zr–3Al, and Ti–35.5Nb–7.3Zr–5.7Ta [32]. These alloys also undergo SIMT during tension and exhibit superelasticity under cyclic loading-unloading. Electron backscatter diffraction analysis of Ti–12Mo after tensile deformation revealed that $\{332\}_{\beta}<113>_{\beta}$ twinning was dominant, accompanied by a small amount of $\{112\}_{\beta}<111>_{\beta}$ twinning. Additionally, needle-like α"-phase was observed within the β matrix, with nanoscale α"-phase precipitates formed in the twinning regions [33]. Combining the XRD results and microstructural observations, the deformation mechanisms of Ti–6Mo–7Cu are proposed to involve dislocation slip, SIMT, and mechanical twinning.

Notably, the superelastic behavior of Ti–6Mo–7Cu differs from that reported in previous studies, where the recovery strain typically decreases after β-phase yielding (at an applied strain of ~5 %) during cyclic loading-unloading tests [34]. In contrast, the recovery strain of Ti–6Mo–7Cu continuously increases until necking occurs. This phenomenon can be attributed to its complex phase composition and synergistic deformation mechanisms. Unlike most solution-treated β-type Ti alloys with SIMT (which typically consist of a single metastable β-phase), Ti–6Mo–7Cu comprises both ω- and β-phases. As a hard phase dispersed in the β-matrix, the ω-phase can enhance the yield strength of

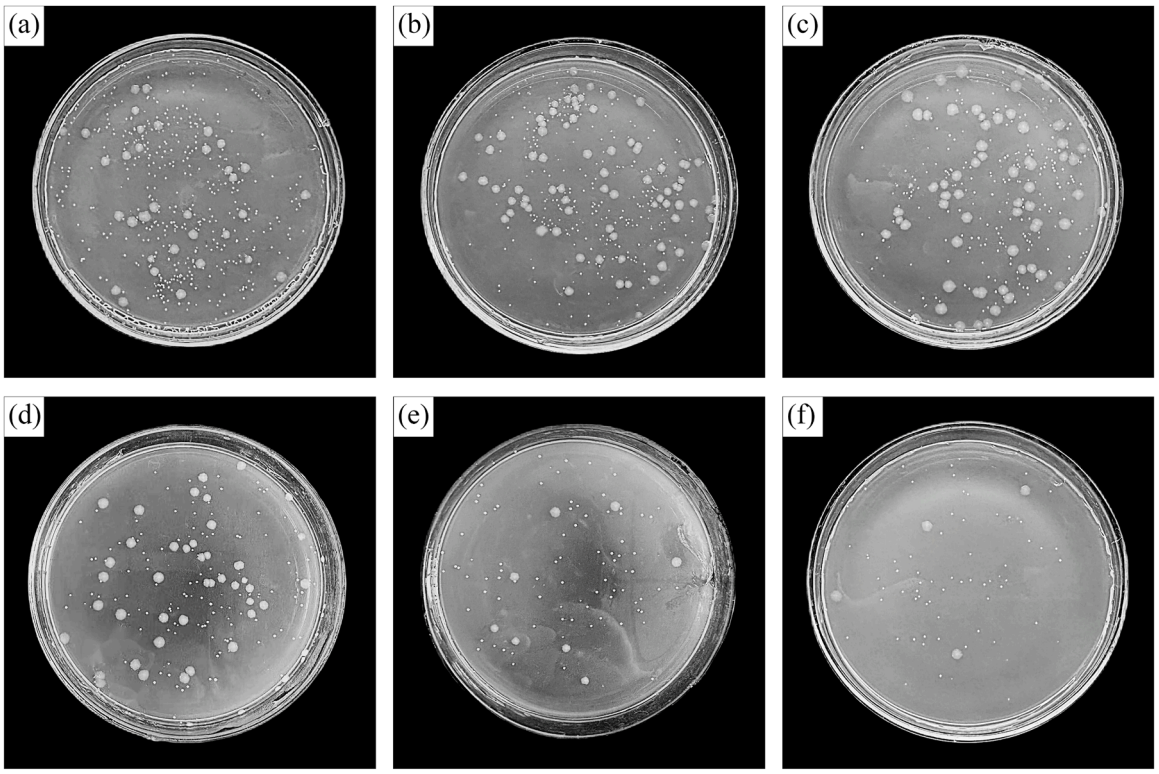

Fig. 11. Morphologies of *S. aureus* corresponding to: (a) CP Ti; (b) Ti–6Mo; (c) Ti–6Mo–1Cu; (d) Ti–6Mo–3Cu; (e) Ti–6Mo–5Cu; (f) Ti–6Mo–7Cu.

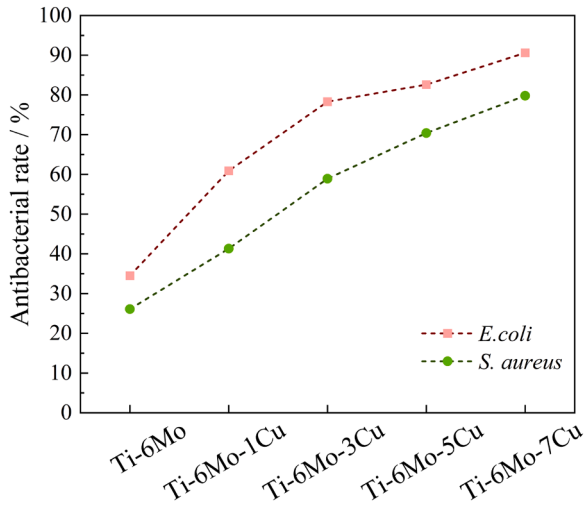

Fig. 12. Variation in antibacterial rates of the Ti–Mo–Cu alloys against *E. coli* and *S. aureus*.

the β-phase, facilitating the induction of more α"-phase during loading. It also restricts the large-scale plastic deformation of the β-phase and induces the formation of α"-phase on a fine scale, thereby contributing to excellent uniform ductility. Additionally, the lattice distortion surrounding the hard ω-phase provides the driving force for the transformation of the induced α"-phase back to the β-matrix during unloading [35]. These effects of the ω-phase enable Ti–6Mo–7Cu to sustain continuous growth of recovery strain until necking, which is distinct from the typical decline in recovery strain observed in some other β-type Ti alloys [34].

The superelastic recovery of β-type Ti alloys is determined by the stability of their β-phase, namely the M_s temperature of the alloy. If the M_s temperature is close to room temperature, the α" phase is prone to stress-induced formation, resulting in a lower initial yield point. Since the α" phase has low strength, plastic deformation readily occurs within it, making it difficult to fully revert to the β-phase during unloading. If the M_s temperature is far below room temperature, the fraction of β-phase that can be stress-induced to transform into α"-phase decreases, leading to limited superelastic recovery. When the M_s temperature is excessively low, superelasticity is completely lost. In this study, the slightly enhanced β-phase stability of Ti–6Mo–7Cu restricts the extent of the β→α" transformation, resulting in a moderate recovery of 2.4 %.

Compared with Ti–Nb-based alloys, Ti–Mo-based alloys typically exhibit a higher E accompanied by superior strength [2], which is consistent with the findings of the present study. The addition of Cu scarcely reduces E, and its solid solution strengthening effect is limited. Consequently, the E, $\sigma_{0.2}$ and σ_b of Ti–Mo–Cu alloys are nearly identical to those of Ti–Mo alloys with comparable $[Mo]_{eq}$. For instance, the Ti–10Mo alloy displays an E of ~77.6 GPa, while that of Ti–10Mo–5Cu remains relatively unchanged at ~74.9 GPa [12]. The E of Ti–6Mo–7Cu is ~85.6 GPa, which is higher than that of Ti–Nb–Cu alloys but lower than those of Ti–Cu binary alloys and Cu-added Ti–6Al–4V [27,36]. Its σ_b exceeds 800 MPa, outperforming other Ti–Nb-based metastable β-type Ti alloys [35].

According to the Ti–Cu binary phase diagram, the maximum solubility of Cu in the β-phase reaches 17.2 % at 1005 °C. Mo, a potent β-phase stabilizer, lowers the α-β transition temperature of the alloy and narrows the (α+β) phase region [2,15]; this reduces the driving force for the eutectoid reaction (β→α+Ti_2Cu) and stabilizes the β-phase at room temperature, thereby inhibiting its decomposition into Ti_2Cu [15,23]. This explains why Ti_2Cu is barely detected via XRD and TEM characterization of Ti–6Mo–7Cu. It is hypothesized that a further increase in Cu content may inhibit the formation of the ω-phase, thereby reducing E. However, excessive Cu addition promotes the precipitation of Ti–Cu intermetallic compounds, which induce brittleness in the alloys [27]. Ti–6Mo–9Cu fractured during hot rolling due to the formation of such Ti–Cu intermetallics, making it impossible to characterize its deformation behavior and mechanical properties.

The Cu^{2+}/Cu redox couple possesses a positive theoretical standard reduction potential, which induces a positive shift in the E_{corr} of the Ti–6Mo–(1, 3, 5, 7)Cu alloys. However, CuO formed during polarization is less stable than TiO_2 [37] and MoO_2 [38], thereby compromising the stability of the passive film [39]. Additionally, the corrosion resistance of Ti alloys is strongly dependent on their phase composition. For α + β-type Ti alloys, corrosion typically initiates at α/β phase boundaries, attributed to the differing passive film formation kinetics of the α- and β-phases, as well as the potential difference between these two phases [40]. Specifically, this potential difference triggers galvanic coupling between the phases, leading to reduced corrosion resistance [41]. Similarly, for the Ti–Zr–Mo–Mn alloys with α" + β-phases, micro-galvanic corrosion occurs at α"/β interfaces, with the α"-phase acting as the anode and undergoing preferential corrosion and dissolution [42]. For the aged Ti–24Nb–2Zr (mol%) alloy, isothermal ω-phase precipitation results in local inhomogeneous elemental distributions, which degrades the stability of the passive film, promotes pitting corrosion, and increases the i_{pp} [35]. Excessive Cu addition also deteriorates corrosion resistance. The formation of Ti–Cu intermetallic compounds creates galvanic cells with either the α- or β-phase, thereby accelerating corrosion [43].

In the present study, the corrosion behaviors of Ti–6Mo–(0, 1, 3, 5, 7) Cu alloys are governed by the combined effects of Cu addition and phase composition. Although Cu addition elevates E_{corr}, it barely enhances the stability of the passive film. The Ti–6Mo–(0, 1, 3)Cu alloys all exhibit a multiphase acicular microstructure. The stability of the initial passive film gradually decreases with increasing Cu content, leading to an increase in i_{pp}. Especially, Ti–6Mo–5Cu, comprising α"-, β-, and ω-phases, exhibits inferior passivation behavior, characterized by the highest i_{pp} and the inability to achieve secondary passivation. Ti–6Mo–7Cu consists mainly of β-phase with dispersed nanosized ω-phase, and its microstructure features equiaxed single β grains. The presence of ω-phase within the β-matrix barely affects the initial passivation behavior of the β-phase but promotes pitting corrosion [44]. The initial passive film of Ti–6Mo–7Cu remains stable prior to pitting, thus exhibiting the lowest i_{pp} among all the alloys investigated. However, the pitting-promoting effect of ω-phase prevents Ti–6Mo–7Cu, along with Ti–6Mo–5Cu, from achieving stable secondary passivation. Nevertheless, all Ti–6Mo–(0, 1, 3, 5, 7)Cu alloys display i_{pp} lower than 100 $\mu A \cdot cm^{-2}$, indicating spontaneous passivation [28].

The antibacterial activity of implant materials is closely associated with the release of antimicrobial agents from their surfaces. Metallic ions (e.g., Ag^+ and Cu^{2+}) can induce the production of reactive oxygen species (ROS); elevated ROS levels trigger oxidative stress within bacterial cells, leading to increased cell membrane permeability or leakage of cellular contents [45]. Such damage to cell membranes and proteins ultimately results in bacterial cell death. The minimum inhibitory concentrations (MIC) of Cu^{2+} against *E. coli* and *S. aureus* are 256 $mg \cdot L^{-1}$ and 448 $mg \cdot L^{-1}$, respectively [46]. In the present study, the maximum Cu^{2+} concentration released from the Ti–6Mo–7Cu alloys was only 6.94 $\mu g \cdot L^{-1}$ after 24 h of immersion, which is much lower than the MIC of Cu^{2+} for *E. coli*. Fortunately, compared with CP Ti and Ti–6Mo, all Ti–6Mo–(1, 3, 5, 7)Cu alloys exhibited enhanced antibacterial activity. This phenomenon is consistent with reports on numerous Cu-containing Ti alloys, which demonstrate strong antibacterial efficacy despite releasing Cu^{2+} at concentrations below the MIC. For example, although the Cu^{2+} concentration of Ti–10Cu immersed in 0.9 % NaCl solution at 37 °C for 120 h was 17.6 $\mu g \cdot L^{-1}$, the corresponding antibacterial rates against *E. coli* and *S. aureus* were 57 % and 79 %, respectively [47]. Ti–6Al–4V–5Cu exhibited an antibacterial rate of 98.6 % against *S. aureus*, with a Cu^{2+} concentration of only ~2.71 $\mu g \cdot L^{-1}$ after 24 h of immersion in 0.9 % NaCl solution [48]. For Ti–7.5Mo–5Cu and Ti–12Mo–5Cu, the Cu^{2+} concentrations after 298 h of immersion in PBS were 2.0 $\mu g \cdot L^{-1}$ and 2.5 $\mu g \cdot L^{-1}$, respectively, while their antibacterial rates against *E. coli* reached 77.0 % and 94.6 %, respectively [49,50]. These phenomena can be attributed to an additional antibacterial mechanism beyond ion release, namely contact killing. Through this mechanism, the materials disrupt the normal function of membrane proteins and ion channels on bacterial cell membranes, leading to bacterial metabolic disorders and ultimately inducing cytoplasmic leakage [9]. The contact-killing antibacterial mechanism of Cu has been validated by evaluating the antibacterial activities of bare Cu and inert polymer-coated Cu against *E. hirae* under conditions of equivalent Cu^{2+} concentrations. The results demonstrated that bare Cu exhibited a much higher antibacterial rate, underscoring the critical role of the contact-killing mechanism [51]. Therefore, the synergistic effect of ion release and contact killing ensures the antibacterial efficacy of Cu-added Ti alloys. Although Ti_2Cu can accelerate Cu^{2+} release, thereby enhancing antibacterial efficiency, embrittlement induced by intermetallic compounds strongly limits the practical application of such alloys [27].

In the present study, Ti–6Mo–7Cu contains the highest Cu content among the Ti–Mo–Cu alloys without the formation of Ti–Cu intermetallic compounds, conferring robust antibacterial activity. Meanwhile, the absence of the brittle Ti_2Cu phase and appropriate β-phase stability endow Ti–6Mo–7Cu with satisfactory mechanical properties coupled with remarkable superelasticity. Its E (~85.6 GPa) is higher than that of Ti–35.3Nb–5.1Ta–7.1Zr (~55.0 GPa), close to that of annealed Ti–15Mo (~78 GPa), and lower than that of annealed Ti–6Al–4V (110–114 GPa) [44]. Its σ_b (~835.9 MPa) is much higher than that of Ti–35.3Nb–5.1Ta–7.1Zr (~596.7 MPa), close to annealed Ti–15Mo (~874 MPa) and annealed Ti–6Al–4V (895–930 MPa). Like these alloys, it exhibits a low i_{pp} with spontaneous passivation [52]. Notably, it also demonstrates desirable antibacterial properties, rendering it a promising candidate for biomedical applications.

5. Conclusion

The following conclusions can be drawn from the above results and discussion:

(1) Cu acts as a β-stabilizing element in Ti–6Mo-based alloys, modifying the phase composition: Ti–6Mo primarily consists of α'- and α"-phases, Ti–6Mo–3Cu comprises α"- and β-phases, and Ti–6Mo–7Cu features a dominant β-phase.
(2) The Ti–6Mo–(0, 1, 3, 5, 7)Cu alloys exhibited high strength with acceptable ductility. Stress-induced martensitic transformation appeared in Ti–6Mo–7Cu with metastable β-phase, enabling a maximum superelastic recovery of ~2.4 %.
(3) The addition of Cu elevates the self-corrosion potential of the alloys. All the Ti–Mo–Cu alloys demonstrate spontaneous passivation behavior with low passivation current densities, ensuring excellent corrosion resistance. The release concentration of Cu^{2+} in PBS elevates with increasing Cu content in the alloys and prolonged immersion time, and all measured concentrations (up to 168 h) fall within the biosafety range.
(4) Cu addition greatly enhances the antibacterial activity of the alloys. As the Cu content increases from 1 % to 7 %, the antibacterial rate against *E. coli* rises from 60.9 % to 90.6 %, and that against *S. aureus* climbs from 41.3 % to 79.8 %—both exhibiting a distinct upward trend. Ti–6Mo–7Cu, with its desirable mechanical properties and high antibacterial efficacy, is a promising candidate for biomedical applications.

CRediT authorship contribution statement

Yichun Zhu: Writing – review & editing, Writing – original draft, Investigation. **Takayoshi Nakano:** Investigation. **Ryosuke Ozasa:** Investigation. **Mitsuo Niinomi:** Investigation. **Kenta Yamanaka:** Investigation. **Masaaki Nakai:** Investigation. **Hao Wang:** Investigation. **Xuyan Liu:** Supervision, Investigation. **Hu Zhao:** Resources, Investigation. **Qiang Li:** Writing – review & editing, Writing – original draft, Supervision, Investigation.

Declaration of Competing Interest

The authors declare that they have no known competing financial interests or personal relationships that could have appeared to influence the work reported in this paper.

Acknowledgements

This work was partially supported by Shanghai Engineering Research Center of Hot Manufacturing, Shanghai Dianji University (No. 18DZ2253400), CREST-Nanomechanics: Elucidation of Macroscale Mechanical Properties Based on Understanding Nanoscale Dynamics for Innovative Mechanical Materials (Grant no.: JPMJCR2194) from the Japan Science and Technology Agency (JST). The authors would like to extend their gratitude to Mr. Tao Xu from Shiyanjia Lab (www.shiyanjia.com) for providing invaluable assistance with the antibacterial tests.

Data availability

No data was used for the research described in the article.

References

[1] G. Senopati, R.A. Rahman Rashid, I. Kartika, et al., Recent development of low-cost β-Ti alloys for biomedical applications: a review, Metals 13 (2) (2023), https://doi.org/10.3390/met13020194.
[2] J.I. Kim, H.Y. Kim, T. Inamura, et al., Shape memory characteristics of Ti–22Nb–(2–8)Zr(at%) biomedical alloys, Mater. Sci. Eng.: A 403 (1–2) (2005) 334–339, https://doi.org/10.1016/j.msea.2005.05.050.
[3] Y. Takemoto, Y. Miyake, T. Senuma, Microstructure and mechanical properties of Ti-Mo and Ti-6Mo-X-Y alloys, J. Jpn. Inst. Met. 73 (9) (2009) 752–757, https://doi.org/10.2320/jinstmet.73.752.
[4] M.D. Juliantoro, G. Senopati, M.S. Dwijaya, et al., Effect of solution treatment and cooling media on the mechanical properties and corrosion behavior of Ti-6Mo-4Cr alloys, Int. J. Corros. Scale Inhib. 12 (2) (2023) 477–488, https://doi.org/10.17675/2305-6894-2023-12-2-6.
[5] M. Hida, K. Miyazawa, S. Tsuruta, et al., Effect of heat treatment conditions on the mechanical properties of Ti-6Mo-4Sn alloy for orthodontic wires, Dent. Mater. J. 32 (3) (2013) 462–467, https://doi.org/10.4012/dmj.2012-118.
[6] F. Guillemot, F. Prima, R. Bareille, et al., Design of new titanium alloys for orthopaedic applications, Med. Biol. Eng. Comput. 42 (1) (2004) 137–141, https://doi.org/10.1007/bf02351023.
[7] C. Sutowo, G. Senopati, A. W Pramono, et al., Microstructures, mechanical properties, and corrosion behavior of novel multi-component Ti-6Mo-6Nb-xSn-xMn alloys for biomedical applications, AIMS Mater. Sci. 7 (2) (2020) 192–202, https://doi.org/10.3934/matersci.2020.2.192.
[8] S. Zhang, Y. Yu, H. Wang, et al., Study on mechanical behavior of Cu-bearing antibacterial titanium alloy implant, J. Mech. Behav. Biomed. Mater. 125 (2022), https://doi.org/10.1016/j.jmbbm.2021.104926.
[9] P. Mahmoudi, M.R. Akbarpour, H.B. Lakeh, et al., Antibacterial Ti–Cu implants: a critical review on mechanisms of action, Mater. Today Bio 17 (2022), https://doi.org/10.1016/j.mtbio.2022.100447.
[10] M. Kostakioti, M. Hadjifrangiskou, S.J. Hultgren, Bacterial biofilms: development, dispersal, and therapeutic strategies in the dawn of the postantibiotic era, Cold Spring Harb. Perspect. Med. 3 (4) (2013), https://doi.org/10.1101/cshperspect.a010306.
[11] N. Høiby, T. Bjarnsholt, M. Givskov, et al., Antibiotic resistance of bacterial biofilms, Int. J. Antimicrob. Agents 35 (4) (2010) 322–332, https://doi.org/10.1016/j.ijantimicag.2009.12.011.
[12] W. Xu, C. Hou, Y. Mao, et al., Characteristics of novel Ti–10Mo-xCu alloy by powder metallurgy for potential biomedical implant applications, Bioact. Mater. 5 (3) (2020) 659–666, https://doi.org/10.1016/j.bioactmat.2020.04.012.
[13] M. Li, Q. Li, J. Yang, et al., Preparation and antibacterial activity of Zn coating on pure Ti with enhanced adhesion, Mater. Today Commun. 38 (2024), https://doi.org/10.1016/j.mtcomm.2024.108149.
[14] M. Chen, E. Zhang, L. Zhang, Microstructure, mechanical properties, bio-corrosion properties and antibacterial properties of Ti–Ag sintered alloys, Mater. Sci. Eng.: C 62 (2016) 350–360, https://doi.org/10.1016/j.msec.2016.01.081.
[15] J.K. Suthar, A. Vaidya, S. Ravindran, Toxic implications of silver nanoparticles on the central nervous system: a systematic literature review, J. Appl. Toxicol. 43 (1) (2022) 4–21, https://doi.org/10.1002/jat.4317.
[16] E. Zhang, F. Li, H. Wang, et al., A new antibacterial titanium–copper sintered alloy: preparation and antibacterial property, Mater. Sci. Eng.: C 33 (7) (2013) 4280–4287, https://doi.org/10.1016/j.msec.2013.06.016.
[17] Y. Yuan, R. Luo, J. Ren, et al., Design of a new Ti-Mo-Cu alloy with excellent mechanical and antibacterial properties as implant materials, Mater. Lett. 306 (2022), https://doi.org/10.1016/j.matlet.2021.130875.
[18] R. Liu, Y. Tang, L. Zeng, et al., In vitro and in vivo studies of anti-bacterial copper-bearing titanium alloy for dental application, Dent. Mater. 34 (8) (2018) 1112–1126, https://doi.org/10.1016/j.dental.2018.04.007.
[19] W.F. Ho, C.P. Ju, J.H. Chern Lin, Structure and properties of cast binary Ti–Mo alloys, Biomaterials 20 (22) (1999) 2115–2122, https://doi.org/10.1016/s0142-9612(99)00114-3.
[20] X.X. Chen, S. Guo, X.Q. Zhao, Phase transformation behavior and mechanical properties of Ti-Mo-Sn alloys, Mater. Sci. Forum 747–748 (2013) 855–859, https://doi.org/10.4028/www.scientific.net/MSF.747-748.855.
[21] W. Ma, S. Guo, G. Liu, et al., Tensile deformation behavior of a solution-treated Ti–33Nb–4Sn alloy with a dual β and α" phases under cyclic loading-unloading, Prog. Nat. Sci.: Mater. Int. 30 (1) (2020) 80–85, https://doi.org/10.1016/j.pnsc.2020.01.008.
[22] E.L. Pang, E.M. Hildyard, L.D. Connor, et al., The effect of quench rate on the β-α″ martensitic transformation in Ti–Nb alloys, Mater. Sci. Eng.: A 817 (2021), https://doi.org/10.1016/j.msea.2021.141240.
[23] F.F. Cardoso, P.L. Ferrandini, E.S.N. Lopes, et al., Ti–Mo alloys employed as biomaterials: effects of composition and aging heat treatment on microstructure and mechanical behavior, J. Mech. Behav. Biomed. Mater. 32 (2014) 31–38, https://doi.org/10.1016/j.jmbbm.2013.11.021.
[24] E. Bertrand, P. Castany, T. Gloriant, Investigation of the martensitic transformation and the damping behavior of a superelastic Ti–Ta–Nb alloy, Acta Mater. 61 (2) (2013) 511–518, https://doi.org/10.1016/j.actamat.2012.09.065.
[25] K.J. Qiu, B.L. Wang, F.Y. Zhou, et al., Comparative in vitro study of Ti-12V-9Sn shape memory alloy with C.P. Ti and Ti-12V alloy for potential biomedical application, J. Mater. Eng. Perform. 21 (12) (2012) 2695–2700, https://doi.org/10.1007/s11665-012-0308-y.
[26] F.Y. Zhou, K.J. Qiu, H.F. Li, et al., Screening on binary Zr–1X (X = Ti, Nb, Mo, Cu, Au, Pd, Ag, Ru, Hf and Bi) alloys with good in vitro cytocompatibility and magnetic resonance imaging compatibility, Acta Biomater. 9 (12) (2013) 9578–9587, https://doi.org/10.1016/j.actbio.2013.07.035.
[27] Z. Wang, B. Fu, Y. Wang, et al., Effect of Cu content on the precipitation behaviors, mechanical and corrosion properties of as-cast Ti-Cu alloys, Materials 15 (5) (2022), https://doi.org/10.3390/ma15051696.
[28] Q. Li, Q. Peng, Q. Huang, et al., Development and characterizations of low-modulus Ti–Nb–Cu alloys with enhanced antibacterial activities, Mater. Today Commun. 38 (2024), https://doi.org/10.1016/j.mtcomm.2024.108402.
[29] L. Fowler, H. Engqvist, C. Öhman-Mägi, Effect of copper ion concentration on bacteria and cells, Materials 12 (22) (2019), https://doi.org/10.3390/ma12223798.
[30] E. Zhang, J. Ren, S. Li, et al., Optimization of mechanical properties, biocorrosion properties and antibacterial properties of as-cast Ti–Cu alloys, Biomed. Mater. 11 (6) (2016), https://doi.org/10.1088/1748-6041/11/6/065001.
[31] P.J. Bania, Beta titanium alloys and their role in the titanium industry, Jom 46 (7) (1994) 16–19, https://doi.org/10.1007/bf03220742.
[32] A.A. Elhadad, L. Romero-Resendiz, M.C. Rossi, et al., Findings and perspectives of β-Ti alloys with biomedical applications: exploring beyond biomechanical and biofunctional behaviour, J. Mater. Res. Technol. 33 (2024) 3550–3618, https://doi.org/10.1016/j.jmrt.2024.09.248.
[33] F. Sun, J.Y. Zhang, M. Marteleur, et al., Investigation of early stage deformation mechanisms in a metastable β titanium alloy showing combined twinning-induced plasticity and transformation-induced plasticity effects, Acta Mater. 61 (17) (2013) 6406–6417, https://doi.org/10.1016/j.actamat.2013.07.019.
[34] X. Ma, X. Wang, Z. Zhang, et al., Tunable shape memory effect and superelasticity in Ti-19.5Zr-10Nb-0.5Fe shape memory alloy wires, J. Mater. Res. Technol. 39 (2025) 5480–5486, https://doi.org/10.1016/j.jmrt.2025.10.221.
[35] Q. Li, J. Li, G. Ma, et al., Influence of ω phase precipitation on mechanical performance and corrosion resistance of Ti–Nb–Zr alloy, Mater. Des. 111 (2016) 421–428, https://doi.org/10.1016/j.matdes.2016.09.026.
[36] T. Aoki, I.C.I. Okafor, I. Watanabe, et al., Mechanical properties of cast Ti-6Al-4V-XCu alloys, J. Oral Rehabil. 31 (11) (2004) 1109–1114, https://doi.org/10.1111/j.1365-2842.2004.01347.x.
[37] C. Zheng, R. Chen, Q. Wang, et al., Great enhancement in corrosion resistance of Ti alloy by Mo element regulating β grain boundary and microstructure, Corros. Sci. 256 (2025), https://doi.org/10.1016/j.corsci.2025.113237.
[38] U. Kumar Sen, A. Shaligram, S. Mitra, Intercalation anode material for lithium ion battery based on molybdenum dioxide, ACS Appl. Mater. Interfaces 6 (16) (2014) 14311–14319, https://doi.org/10.1021/am503605u.
[39] Y. Yang, F. Li, J. Ren, et al., Characterization on corrosion and antibacterial properties of a new functionally graded porous Ti–Mo–Cu alloys with improved cytocompatibility, Vacuum 215 (2023), https://doi.org/10.1016/j.vacuum.2023.112353.
[40] M. Atapour, A.L. Pilchak, G.S. Frankel, et al., Corrosion behavior of β titanium alloys for biomedical applications, Mater. Sci. Eng.: C 31 (5) (2011) 885–891, https://doi.org/10.1016/j.msec.2011.02.005.
[41] F. Yu, O. Addison, A. Davenport, Temperature-dependence corrosion behavior of Ti6Al4V in the presence of HCl, Front. Mater. 9 (2022), https://doi.org/10.3389/fmats.2022.880702.
[42] H. Liu, J. Yang, X. Zhao, et al., Microstructure, mechanical properties and corrosion behaviors of biomedical Ti-Zr-Mo-xMn alloys for dental application, Corros. Sci. 161 (2019), https://doi.org/10.1016/j.corsci.2019.108195.
[43] S. Guo, Y. Lu, S. Wu, et al., Preliminary study on the corrosion resistance, antibacterial activity and cytotoxicity of selective-laser-melted Ti6Al4V- x Cu alloys, Mater. Sci. Eng.: C 72 (2017) 631–640, https://doi.org/10.1016/j.msec.2016.11.126.

[44] M. Niinomi, Mechanical properties of biomedical titanium alloys, Mater. Sci. Eng.: A 243 (1–2) (1998) 231–236, https://doi.org/10.1016/s0921-5093(97)00806-x.
[45] M. Godoy-Gallardo, U. Eckhard, L.M. Delgado, et al., Antibacterial approaches in tissue engineering using metal ions and nanoparticles: from mechanisms to applications, Bioact. Mater. 6 (12) (2021) 4470–4490, https://doi.org/10.1016/j.bioactmat.2021.04.033.
[46] E. Zhang, X. Wang, M. Chen, et al., Effect of the existing form of Cu element on the mechanical properties, bio-corrosion and antibacterial properties of Ti-Cu alloys for biomedical application, Mater. Sci. Eng.: C 69 (2016) 1210–1221, https://doi.org/10.1016/j.msec.2016.08.033.
[47] J. Liu, F. Li, C. Liu, et al., Effect of Cu content on the antibacterial activity of titanium–copper sintered alloys, Mater. Sci. Eng.: C 35 (2014) 392–400, https://doi.org/10.1016/j.msec.2013.11.028.
[48] Z. Ma, L. Ren, R. Liu, et al., Effect of heat treatment on Cu distribution, antibacterial performance and cytotoxicity of Ti–6Al–4V–5Cu alloy, J. Mater. Sci. Technol. 31 (7) (2015) 723–732, https://doi.org/10.1016/j.jmst.2015.04.002.
[49] D. Xu, T. Wang, S. Wang, et al., Antibacterial effect of the controlled nanoscale precipitates obtained by different heat treatment schemes with a Ti-based nanomaterial, Ti–7.5Mo–5Cu alloy, ACS Appl. Bio Mater. 3 (9) (2020) 6145–6154, https://doi.org/10.1021/acsabm.0c00716.
[50] D. Xu, Z. Lu, T. Wang, et al., Novel Ti-based alloys prepared with different heat treatment strategies as antibacterial biomedical implants, Mater. Des. 205 (2021), https://doi.org/10.1016/j.matdes.2021.109756.
[51] S. Mathews, M. Hans, F. Mücklich, et al., Contact killing of bacteria on copper is suppressed if bacterial-metal contact is prevented and is induced on iron by copper ions, Appl. Environ. Microbiol. 79 (8) (2013) 2605–2611, https://doi.org/10.1128/aem.03608-12.
[52] W.-F. Ho, A comparison of tensile properties and corrosion behavior of cast Ti–7.5Mo with c.p. Ti, Ti–15Mo and Ti–6Al–4V alloys, J. Alloy. Compd. 464 (s 1–2) (2008) 580–583, https://doi.org/10.1016/j.jallcom.2007.10.054.